

Full Length Article

H₂O₂ formation mechanisms on the (112) and (310) facets of SnO₂ via water oxidation reaction with the participation of Bicarbonate: DFT and experimental Investigations

Wenlong Guo^a, Yinqiong Xie^a, Shi Tang^a, Bo Yu^b, Xin Lian^{b,*}, Graeme Henkelman^c, Xi Liu^{a,*}

^a Chongqing Key Laboratory of Inorganic Functional Materials, College of Chemistry, Chongqing Normal University, Chongqing 401331, PR China

^b College of Chemistry and Chemical Engineering, Chongqing University of Science and Technology, Chongqing, 401331, PR China

^c Department of Chemistry and the Oden Institute for Computational Engineering and Sciences, The University of Texas, Austin, TX 78712, United States



ARTICLE INFO

Keywords:

H₂O₂
Water oxidation
Bicarbonate
SnO₂
(112) and (310) surfaces

ABSTRACT

The H₂O₂ formation mechanisms on the (112) and (310) facets of SnO₂ via the water oxidation reaction (WOR) with participation of bicarbonate are investigated by density functional theory calculations and electrochemical measurements. Both computational and experimental results show that H₂O₂ generation is hindered on the surfaces of SnO₂ in the absence of HCO₃⁻ species. In contrast, more H₂O₂ is detected for SnO₂ films tested in HCO₃⁻ aqueous solution than those measured in non-bicarbonate electrolyte. Nevertheless, our kinetic simulations suggest that the co-adsorption of HCO₃⁻ species adjacent to H₂O on the (112) and (310) surfaces of SnO₂ do not effectively promote the two-electron WOR to form H₂O₂. Considering that the H₂O₂ production scales linearly with the concentration of HCO₃⁻, bicarbonate is likely to directly participate in the process of H₂O₂ generation as a catalytic medium. That is, the mechanism that H₂O₂ is formed through the hydrolyzation of HCO₄⁻ that is produced by the peroxidation of HCO₃⁻ is likely. Our calculations show that H₂O₂ is formed through this route on both (112) and (310) facets of SnO₂. In addition, the (112) surface of SnO₂ is kinetically favored for H₂O₂ generation compared to the (310) facet.

1. Introduction

Hydrogen peroxide (H₂O₂) is an important chemical with many uses, such as medical sterilization, chemical product synthesis, environmental pollution treatment, and the electronics industry.[1–3] Among the methods for H₂O₂ synthesis, the electrocatalytic processes has been widely favored by researchers due to its environmental friendliness, high safety, and in-situ synthesis.[4–8] Compared with the H₂O₂ production by reducing oxygen at the cathode,[49–53] the generation of H₂O₂ via two-electron water oxidation reaction (2e⁻ WOR) at the anode has encouraging advantages and attractive prospects.[9–12] This procedure allows the production of value-added H₂O₂ at the anode and simultaneously evolution of H₂ at the cathode. Typically, the anode materials currently used for the generation of H₂O₂ are metal oxides, including MnO_x,[13] WO₃,[14,15] SnO₂,[14] TiO₂,[14–16], ZnO, [17,18] BiVO₄,[19–24] CaSnO₃,[25,26] Mo:Bi₂WO₆,[27] and TiO_{2-x}. [48] This is primarily because metal oxides exhibit distinctive stability under the oxidation potential in the aqueous solution. It is worth noting

that H₂O₂ preparation based on these oxides through electrochemical or photoelectrochemical processes almost requires bicarbonate (HCO₃⁻) salt as the electrolyte.[14–27] This suggests that HCO₃⁻ species play an important role in the production of H₂O₂.

Experimentally, Fuku and coauthors studied H₂O₂ generation on metal oxides via the 2e⁻ WOR and proposed a mechanism where H₂O₂ is a product of the hydrolysis of percarbonates species (HCO₄⁻ and C₂O₈²⁻) which are formed by the oxidation of HCO₃⁻ at high applied voltages on the electrodes.[15,28] In their work, the KHCO₃ electrolyte can significantly facilitate oxidative H₂O₂ production compared with other electrolytes including LiSO₄, NaClO₄, H₃BO₃ + KOH, K₂CO₃, and a phosphate buffer. Subsequently, the experimental result that HCO₃⁻ electrolyte can promote the generation of H₂O₂ via the 2e⁻ WOR on metal oxides was confirmed by a number of other studies.[27,29] Very recently, Zheng's group investigated the role of bicarbonate-based electrolyte species (HCO₃⁻ and CO₃²⁻) for 2e⁻ WOR using a combination of electrochemical and spectroscopic methods with BiVO₄ as an anode.[30] The findings of these authors show that HCO₃⁻/HCO₄⁻ serves

* Corresponding authors.

E-mail addresses: daisylilian0121@163.com (X. Lian), xliu@cqu.edu.cn (X. Liu).

<https://doi.org/10.1016/j.apsusc.2022.153634>

Received 22 February 2022; Received in revised form 8 May 2022; Accepted 9 May 2022

Available online 11 May 2022

0169-4332/© 2022 Elsevier B.V. All rights reserved.

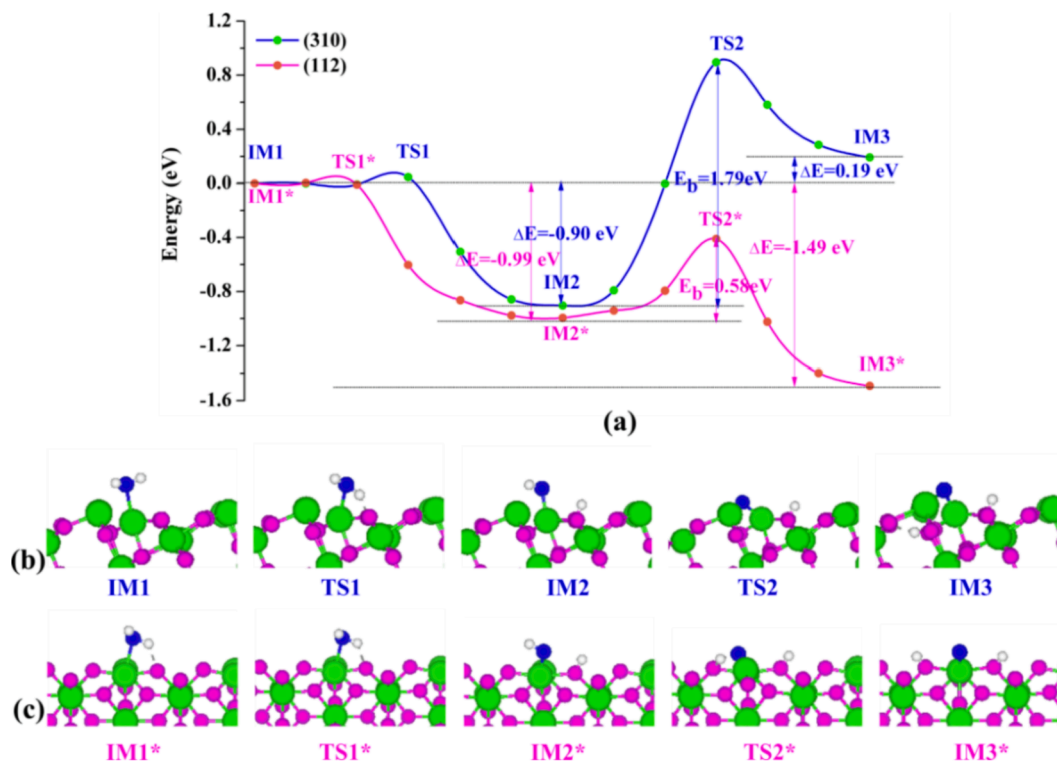


Fig. 1. (a) MEP plots for the pathway of $^*\text{H}_2\text{O} \rightarrow ^*\text{OH} + ^*\text{H} \rightarrow ^*\text{O} + 2^*\text{H}$ on the (310) and (112) facets of SnO_2 in the absence of HCO_3^- species. The side view of the intermediates and transition states along the paths on the (310) (b) and (112) surfaces (c). The corresponding top views are shown in Figure S5. Sn and O are depicted as green and magenta spheres respectively. The adsorbed O and H atoms are blue and white respectively.

as a redox catalyst for H_2O_2 production in KHCO_3 electrolytes. Theoretically, Nørskov and coauthors show that the selectivity trends of an electrocatalyst between the $2e^-$ WOR and $4e^-$ WOR can be evaluated based on the free energy of adsorbed OH^* group.[14,31] Using density functional theory (DFT) calculations, the authors proposed that the ZnO (10 $\bar{1}$ 0) surface and BiVO_4 doping with optimal concentrations of gadolinium are effective catalysts for $2e^-$ WOR; these predictions were confirmed experimentally.[17,20] Khushalani *et al.* studied the co-adsorption of H_2O_2 and HCO_3^- species and their calculations show that the adsorption behavior of HCO_3^- species have different effects on the stability of H_2O_2 molecules on the (−1 2 1) and (0 4 0) planes of BiVO_4 . [19] Despite these efforts, the role of HCO_3^- , and especially the mechanism of adsorption and peroxidation of the HCO_3^- species on the catalyst surface and its influence mechanism on the generation of H_2O_2 , needs to be further explored.

In this work, using DFT calculations and electrochemical measurements, we investigate the H_2O_2 generation mechanisms from the aspect of kinetics on the (112) and (310) surfaces of SnO_2 . SnO_2 has been demonstrated to be a potential candidate for H_2O_2 production via the $2e^-$ WOR.[14] SnO_2 is the main component of the coating of the conductive glass which has been widely used in the field of catalysis. [29] The H_2O_2 formation pathways and energy barriers with and without the participation of HCO_3^- species are scrutinized. H_2O_2 production in bicarbonate and non-bicarbonate electrolytes for SnO_2 films are detected after a period of chronoamperometry tests. Specifically, the peroxidation of HCO_3^- and the hydrolyzation of HCO_4^- species are investigated on the (112) and (310) facets of SnO_2 . Moreover, the catalytic activities of the (112) and (310) crystal planes of SnO_2 for H_2O_2 generation are compared. Our work has deepened the understanding of the role of HCO_3^- in H_2O_2 production and provided some suggestions for the design and synthesis of catalysts for $2e^-$ WOR.

2. Computational and experimental methods

2.1. Computational details

The Vienna ab initio simulation package (VASP)[32–34] using a plane wave basis set with a cut-off energy of 420 eV are used for all calculations.[35,36] The electronic-correlation energies are calculated using the generalized gradient approximation functional of the Perdew–Burke–Ernzerhof form.[37,38] ($2 \times 3 \times 1$) and ($3 \times 2 \times 1$) Monkhorst-Pack grids for the (2×2) surface unit cells of the SnO_2 (112) and (310) surfaces were used for Brillouin-zone integration, respectively.[39] Slab structures included three layers where the bottom layer was fixed and the top layers were free to relax until all force components dropped below 0.01 eV/Å. Periodic slabs along the z-direction were separated by a vacuum region of 15 Å. The climbing-image nudged elastic band (CI-NEB) method is used to locate the transition states (TSs). [40] The adsorption energies of H_2O and HCO_3^- species are calculated as follows:

$$E_{ads} = E_{\text{SnO}_2/(\text{H}_2\text{O or HCO}_3^-)} - (E_{\text{SnO}_2} + (E_{\text{H}_2\text{O}} \text{ or } E_{\text{HCO}_3^-})) \quad (1)$$

where $E_{\text{SnO}_2/(\text{H}_2\text{O or HCO}_3^-)}$ is the total energy of the SnO_2 - H_2O or SnO_2 - HCO_3^- system, E_{SnO_2} is the energy of the substrate, and $E_{\text{H}_2\text{O}}$ and $E_{\text{HCO}_3^-}$ is the energy of an isolated water molecule and an isolated bicarbonate, respectively. The reaction pathways for $4e^-$ WOR and $2e^-$ WOR are as follows.[31,41,42].

$4e^-$ WOR:



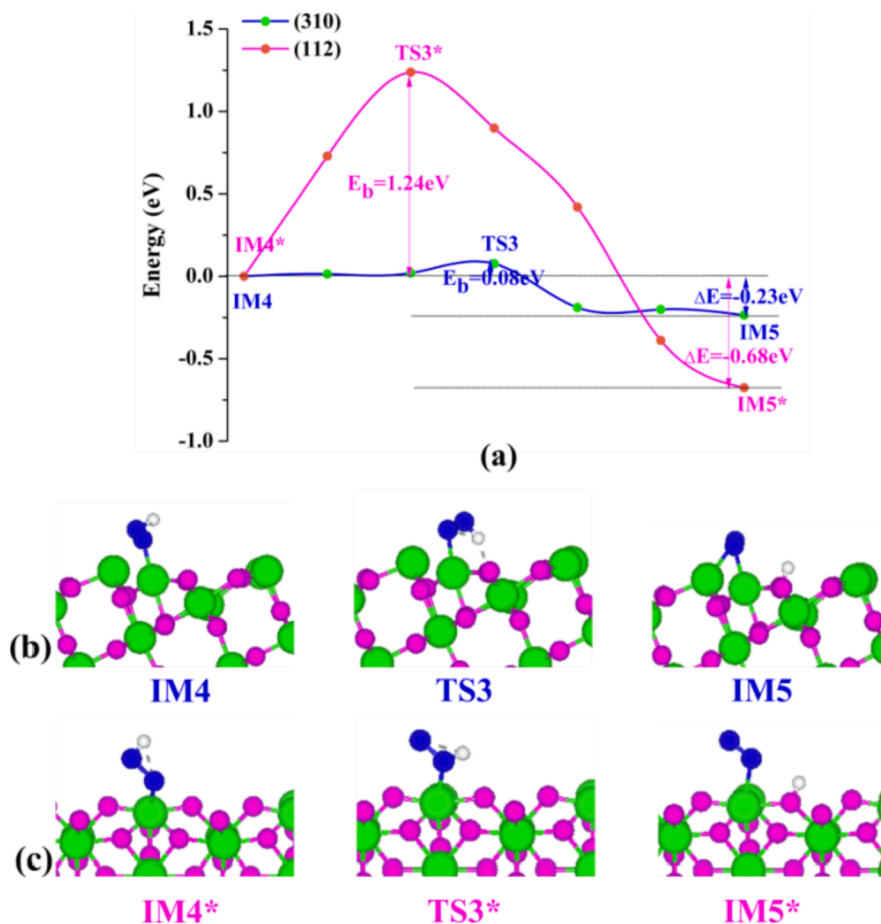


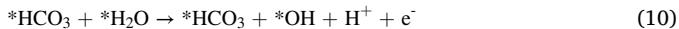
Fig. 2. (a) MEP plots for the pathway of $^*\text{OOH} \rightarrow ^*\text{OO} + ^*\text{H}$ on the (310) and (112) facets of SnO_2 in the absence of HCO_3^- species. The side view of the intermediates and transition states along the paths on the (310) (b) and (112) surfaces (c). The corresponding top views are shown in Figure S6. Sn and O are depicted as green and magenta spheres respectively. The adsorbed O and H atoms are blue and white respectively.



2e^- WOR:



The reaction pathways for the peroxidation of HCO_3^- species and the hydrolyzation of HCO_4^- groups are as follows. [2,3,43].



where * represents an active surface site and the group with the * represents a group adsorbed on an active surface site.

2.2. Material synthesis, characterization, and testing

All chemicals were obtained from commercial sources and used without further purification. The SnO_2 nanosheets were synthesized according to the literature. [44] Briefly, 0.2 g of urea (J.T.Baker, 99.0–100.5%) was dissolved into a mixed solution of 35 mL deionized water and 15 mL ethanol. 10 mM SnCl_2 (Adamas, 99%+) was then

added into the above solution. Next, 1 mL of 6 M NaOH was slowly added into the solution. Then, 17 mL of the solution was transferred into a Teflon-lined autoclave. The autoclave was kept at 180 °C for 18 h and naturally cooled to room temperature. The product was centrifuged and washed three times with a rotation speed of 10,000 rpm and a time of 10 min. The washed sediments were dispersed into the deionized water again and the gray sediments were removed after 5 min to obtain an upper layer of a yellow–brown suspension. The suspension was centrifuged and washed three times (10,000 rpm, 10 min). Finally, the product was dried in an oven at 60 °C for 12 h. X-ray diffraction (XRD) measurements with $\text{Cu K}\alpha$ X-rays (SHIMADU) were used to determine the phases of the synthesized nanosheets. X-ray photoelectron spectroscopy (XPS, Escalab) was conducted to detect the electron binding energies of Sn and O elements of the SnO_2 nanosheets. The morphology of the SnO_2 nanosheets was measured using a scanning electron microscope (SEM, FEI Inspect F50 (FSEM)). For electrochemical testing, the SnO_2 nanosheets were spin-coated on fluoride-doped tin oxide (FTO) conductive glass which had been ultrasonically cleaned in deionized water and ethanol for 30 min. SnO_2 nanosheets were dispersed in isopropanol and ultrasonically treated for 30 min. The speed of spin coating was 500 rpm for 5 s and then 2500 rpm for 20 s. The obtained film was annealed in a box furnace at 350 °C for 2 h to remove residue and for better attachment.

An H-type three-electrode quartz cell was used to conduct the electrochemical measurements with an Ag/AgCl (in saturated KCl) as the reference electrode and a Pt wire as the counter electrode. The SnO_2 film was applied as the working electrode with a reaction area of 4 cm^2 . The anode and cathode were separated using a Nafion ion exchange

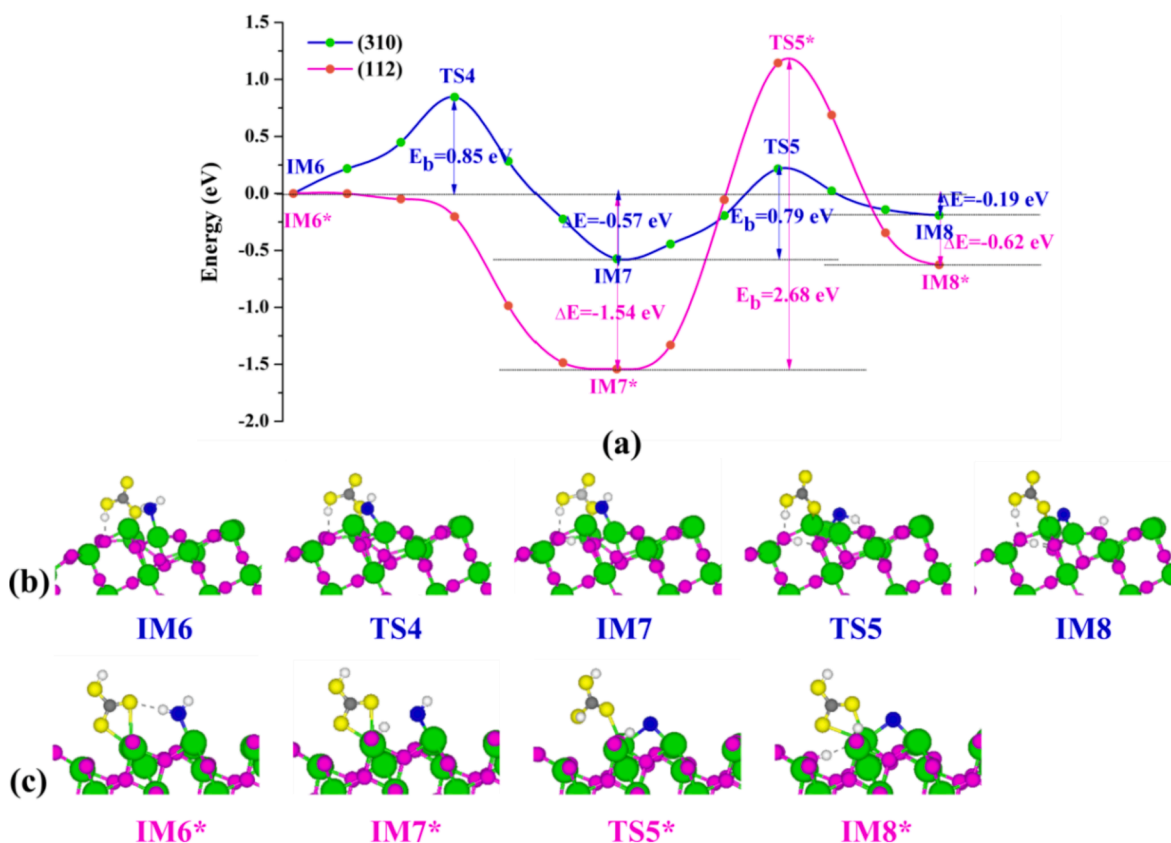


Fig. 3. (a) MEP plots for the pathway of $^*\text{H}_2\text{O} \rightarrow ^*\text{OH} + ^*\text{H} \rightarrow ^*\text{O} + 2^*\text{H}$ on the (310) and (112) facets of SnO_2 in the presence of HCO_3^- species. The side view of the intermediates and transition states along the paths on the (310) (b) and (112) surfaces (c). The corresponding top views are shown in Figure S7. Sn and O are depicted as green and magenta spheres, respectively. The adsorbed C, O, and H atoms in HCO_3^- group are grey, yellow and white, respectively. The adsorbed O and H atoms in H_2O molecule are blue and white respectively.

membrane; the volume of electrolyte was 30 mL. A CHI 760E workstation was used to perform all electrochemical tests. The Nernst equation was applied to calculate the potentials versus reversible H_2 electrode (RHE) as follows:

$$E_{\text{RHE}} = E_{\text{Ag/AgCl}} + 0.0591 \times \text{pH} + E_{\text{Ag/AgCl}}^0 (0.197 \text{ V}).$$

The standard test strips and the KMnO_4 reaction method combined with a UV-vis spectrophotometer were used to measure H_2O_2 concentrations. The amount of H_2O_2 was calculated by the consumption of MnO_4^- whose absorption wavelength is selected as 525 nm.

3. Results and discussions

We first calculate the reaction pathways and energy barriers for $4e^-$ -WOR and $2e^-$ -WOR on the (112) and (310) surfaces of SnO_2 in the absence of HCO_3^- . The geometric and structural descriptions of the optimized bulk SnO_2 , SnO_2 (112), and SnO_2 (310) facets are shown in Figure S1. The minimum energy paths (MEP) and the intermediates and transition states on the (112) and (310) facets for the dehydrogenation of the adsorbed H_2O are shown in Fig. 1. On the (112) and (310) facets, the splitting of $^*\text{H}_2\text{O}$ into $^*\text{H}$ and $^*\text{OH}$ requires almost no energy barrier, indicating that this reaction on the two surfaces is spontaneous (Fig. 1a). The energies of the final states of this reaction are 0.99 and 0.90 eV lower than the initial states for the (112) and (310) surfaces, respectively. For the subsequent scission of the $^*\text{OH}$ species, the barrier on the (310) facet is much higher than that on the (112) facet, which are 1.79 and 0.58 eV respectively. The breaking of the O-H bond on the (310) facet is endothermic; the energy of the final state is 1.09 eV higher than the initial state. In contrast, the breaking of the O-H bond on the (112) facet is exothermic; the energy of the final state is 0.50 eV lower than the

initial state. This suggests that the cleavage of the $^*\text{OH}$ group on the (310) facet is more difficult than on the (112) facet. As shown in Fig. 1b and c, on both facets, H_2O is adsorbed on the top site of the Sn atom by the O. Different possibilities of adsorbing H_2O on these surfaces have been investigated and the most stable configurations are used for subsequent calculations (see Figure S1 and Table S1). Through dehydrogenation, a proton of H_2O moves to the adjacent lattice O and then the second proton in $^*\text{OH}$ migrates to another lattice O. The hydroperoxy species $^*\text{OOH}$ is formed by bonding another H_2O molecule from the solution to the metal-oxo species ($^*\text{O}$), accompanied by the loss of a proton from H_2O . [41] For both facets, the $^*\text{OOH}$ group is adsorbed on the surface at O sites, and the H atom migrates to the nearby O atom in the lattice as the O-H bond breaks (Fig. 2b and c). The energy barriers for the $^*\text{OOH}$ dehydrogenation on the (112) and (310) surfaces are significantly different: 1.24 and 0.08 eV, respectively (Fig. 2a). This indicates that the dehydrogenation of $^*\text{OOH}$ to generate $^*\text{OO}$ species on the (112) surface is hindered. In the proposed $4e^-$ -WOR mechanism, the dehydrogenation of $^*\text{OH}$ is calculated to be the rate-limiting step for the (310) surface. Different from the (310) surface, the rate-limiting step on the (112) facet is the dehydrogenation of $^*\text{OOH}$. Judging from the energy barriers of the rate-determining steps, these two surfaces of SnO_2 are not kinetically favorable for the $4e^-$ -WOR. These conclusions are consistent with the relatively low observed performance of SnO_2 as an electrocatalyst for oxygen evolution through WOR. [45].

For comparison, we calculate the $2e^-$ -WOR to generate $^*\text{H}_2\text{O}_2$ in the absence of HCO_3^- . Not unexpectedly, the H_2O_2 molecule does not stably adsorb on the (112) and (310) surfaces and instead decomposes spontaneously; H_2O_2 is extremely unstable on these surfaces and it is difficult to generate H_2O_2 through the $2e^-$ -WOR on SnO_2 in an actual electrocatalytic process. SnO_2 nanosheets have been synthesized and

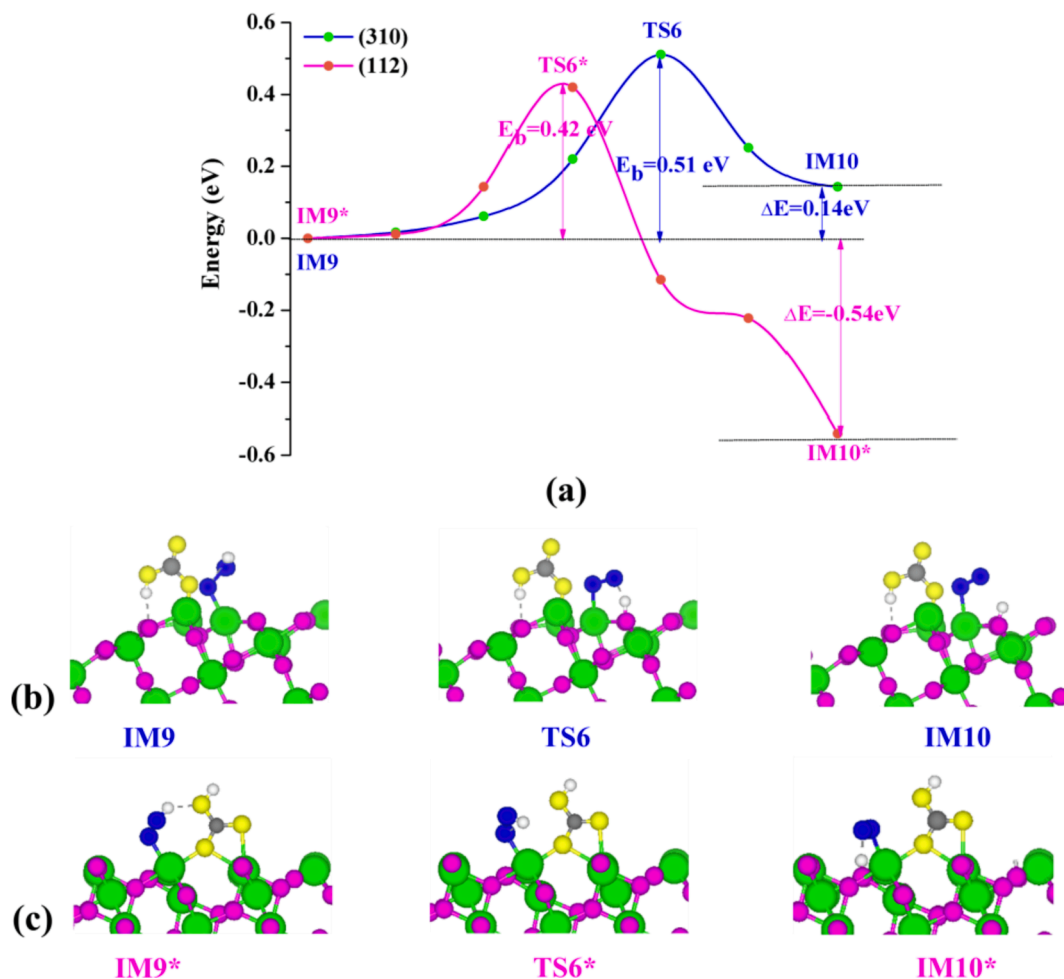


Fig. 4. (a) MEP plots for the pathway of $^*\text{OOH} \rightarrow ^*\text{OO} + ^*\text{H}$ on the (310) and (112) facets of SnO_2 in the presence of HCO_3^- species. The side view of the intermediates and transition states along the paths on the (310) (b) and (112) surfaces (c). The corresponding top views are shown in Figure S8. Sn and O are depicted as green and magenta spheres respectively. The adsorbed C, O, and H atoms in HCO_3^- group are grey, yellow and white, respectively. The adsorbed O and H atoms are blue and white respectively.

coated on FTO conductive glass to conduct electrochemical measurements. The XRD spectrum of the SnO_2 nanosheets matches the main characteristic peaks of SnO_2 (PDF#41-1445), indicating that the phase of the prepared SnO_2 nanosheets is adequately pure (Figure S2). XPS spectra of Sn 3d and O 1s collected from the SnO_2 nanosheets are shown in Figure S3. The binding energies of Sn 3d_{5/2} and Sn 3d_{3/2} locate at 486.7 and 495.2 eV respectively, confirming the presence of Sn^{4+} ions. [46] Typical morphologies of SnO_2 nanosheets synthesized by the hydrothermal method are shown in Figure S4. We selected several non-bicarbonate solutions (Na_2SO_4 , K_2HPO_4 , and KH_2PO_4) to test the performances of SnO_2 films for electrocatalytic H_2O_2 production. As shown in Fig. 5d, after 15 min of the chronoamperometry test, the H_2O_2 concentrations in the electrolytes are negligibly small.

From the above discussion, H_2O_2 generation through the $2e^-$ WOR on the (112) and (310) surfaces are kinetically unfavorable compared with the O_2 evolution via the $4e^-$ WOR without the participation of HCO_3^- . These calculation and test results are consistent with the experimental observations of various metal oxides for H_2O_2 production tested in non-bicarbonate solutions in previous work. [15,29] In order to explore the role of bicarbonate, the HCO_3^- group is introduced onto the (112) and (310) surfaces of SnO_2 . Similarly, the $4e^-$ WOR and $2e^-$ WOR on the (112) and (310) in the presence of $^*\text{HCO}_3^-$ are calculated. The pathways and energy barriers for the dehydrogenation of H_2O are calculated and the MEP plots and the involved intermediates and transition structures on the (112) and (310) surfaces are shown in Fig. 3. The HCO_3^- species is

adsorbed on the top-site of a Sn atom with the O end and the H_2O molecule adsorbed on the adjacent Sn atom (Fig. 3b and c). Various adsorption sites for HCO_3^- on the (112) and (310) surfaces have been considered, the most stable of which are used as the subsequent reactants (see Figure S1 and Table S1). As in the absence of $^*\text{HCO}_3^-$, the process of removing the first H atom from $^*\text{H}_2\text{O}$ occurs without an energy barrier on the (112) surface. As shown in Fig. 3a, different from the (112) surface, the $^*\text{H}_2\text{O}$ dehydrogenation requires an energy barrier of 0.85 eV on the (310) surface. Similar to the situation with no bound $^*\text{HCO}_3^-$, the processes of splitting $^*\text{H}_2\text{O}$ into $^*\text{H}$ and $^*\text{OH}$ on the (112) and (310) surfaces with the co-adsorption of the HCO_3^- group are exothermic. The energies of the final states of this process are 1.54 and 0.57 eV lower than the initial states for the (112) and (310) facets, respectively. The dehydrogenation of $^*\text{OH}$ changes from exothermic to endothermic on the (112) surface with high energy barrier of 2.68 eV, indicating that, in the presence of $^*\text{HCO}_3^-$, the breaking of $^*\text{OH}$ on the (112) surface becomes relatively difficult. On the (310) surface, the energy barrier for the $^*\text{OH}$ dehydrogenation decreases from 1.79 to 0.79 eV after introducing $^*\text{HCO}_3^-$ although this process is still endothermic by 0.38 eV. As shown in Fig. 4, the structures for the co-adsorption of $^*\text{HCO}_3^-$ and $^*\text{OOH}$ are derived from the products after H_2O dehydrogenation in the last step. For the dehydrogenation of $^*\text{OOH}$, the energy barrier lowers from 1.24 to 0.42 eV on the (112) surface. In contrast, the energy barrier for $^*\text{OOH}$ dehydrogenation to $^*\text{OO}$ and $^*\text{H}$ on the (310) surface increases from 0.08 to 0.51 eV, changing the process from

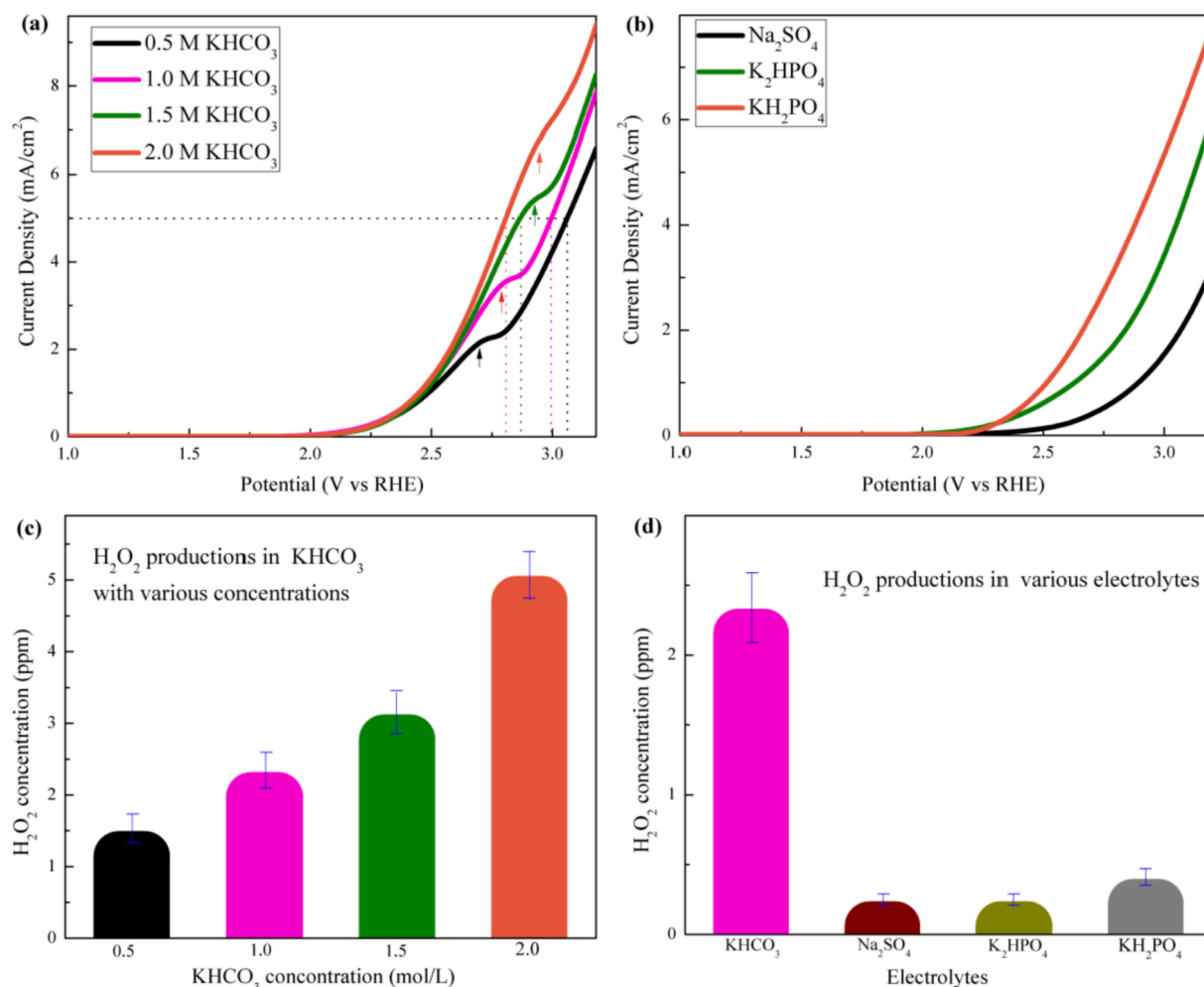


Fig. 5. (a) LSV for SnO₂ films tested in KHCO₃ electrolytes with various concentrations. The pH values are around 8.3 of these electrolytes. (b) LSV for SnO₂ films tested in various non-bicarbonate aqueous solution with a concentration of 1 mol/L. The pH values of Na₂SO₄, K₂HPO₄, and KH₂PO₄ are 6.7, 9.2, and 4.3, respectively. (c) The detected H₂O₂ concentrations in different concentrations of KHCO₃ at 3.08 V vs RHE after 15 min reaction. (d) The detected H₂O₂ concentrations in different electrolytes at 3.08 V vs RHE after 15 min of reaction time.

exothermic to endothermic. Typically, the co-adsorption of *HCO₃ makes the cleavage of *OH on the (310) surface easier, while it makes this reaction more difficult on the (112) surface. The rate-determining steps for 4e⁻WOR on the (112) and (310) surfaces are changed to be the dehydrogenations of *OH and *H₂O, respectively. By calculating the adsorption energies, it is found that the existence of *HCO₃ increases the adsorption energy of H₂O on the (112) surface from -0.83 to -1.12 eV, while decreases the adsorption energy of H₂O on the (310) surface from -2.53 to -1.14 eV. Taking into account the differences in the energy barriers and reaction characteristics for the dehydrogenations of *H₂O, *OH, and *OOH on the (112) and (310) surfaces with and without *HCO₃, it can be speculated that *HCO₃ affects the water oxidation kinetics by changing the adsorptions of H₂O and intermediates.

For 2e⁻WOR in the presence of *HCO₃, stable structures of H₂O₂ and suitable pathways are not found in this work. Therefore, it could be concluded that the co-adsorption of *HCO₃ has no obvious promotion effect on the H₂O₂ generation via 2e⁻WOR although *HCO₃ would affect the oxidation kinetics of H₂O on SnO₂. However, decent production rates and Faradic efficiencies of H₂O₂ have been observed for SnO₂ and SnO₂-based anodes tested in bicarbonate aqueous solution in previous work.[14,29] In this work, the H₂O₂ production of SnO₂ film in bicarbonate and non-bicarbonate solutions are measured. As expected, overwhelming H₂O₂ concentration is detected in KHCO₃ after 15 min reaction at 3.08 V vs RHE compared to those tested in non-bicarbonate solutions (Fig. 5d). In addition, as the concentration of HCO₃⁻ in the

electrolyte increases, the generation of H₂O₂ increases linearly (Fig. 5c). A comparison of the H₂O₂ production rate between our work and other reports of SnO₂ is provided in Table S1. The linear sweep voltammetry (LSV) plots for SnO₂ films tested in KHCO₃ solution with various concentrations are tested and shown in Fig. 5a. Note that the current density gradually increases as the concentration of HCO₃⁻ in the solution increases. These results demonstrate that HCO₃⁻ plays a key role in the formation of H₂O₂. Combined with the calculation results, HCO₃⁻ is likely to directly participate in the formation of H₂O₂ on the SnO₂ surface. Considering the current proposed mechanism that H₂O₂ is generated by the hydrolysis of HCO₄⁻ which is derived from the electrochemical oxidation of HCO₃⁻, [15,28,30] the conjecture that HCO₃⁻ acts as a catalytic medium in the generation of H₂O₂ is understandable. In fact, HCO₄⁻ has been detected in KHCO₃ aqueous solution after a period of electrochemical measurements in a recent work.[47] In addition, oxidation peaks are observed in the LSV curves of the SnO₂ films tested in KHCO₃ electrolyte with various concentrations, which indicates the oxidation of HCO₃⁻ to HCO₄⁻ (Fig. 5a).[30] In contrast, there are no similar oxidation peaks in the LSV plots tested in the non-bicarbonate solutions (Fig. 5b).

Based upon these results, it is necessary to investigate the pathways and energy barriers for the peroxidation of *HCO₃ and the hydrolyzation of *HCO₄ species on the surfaces of SnO₂. The peroxidation process in which *HCO₃ interacts with the *O species derived from the *H₂O dehydrogenation to form *HCO₄ on the (112) and (310) facets is

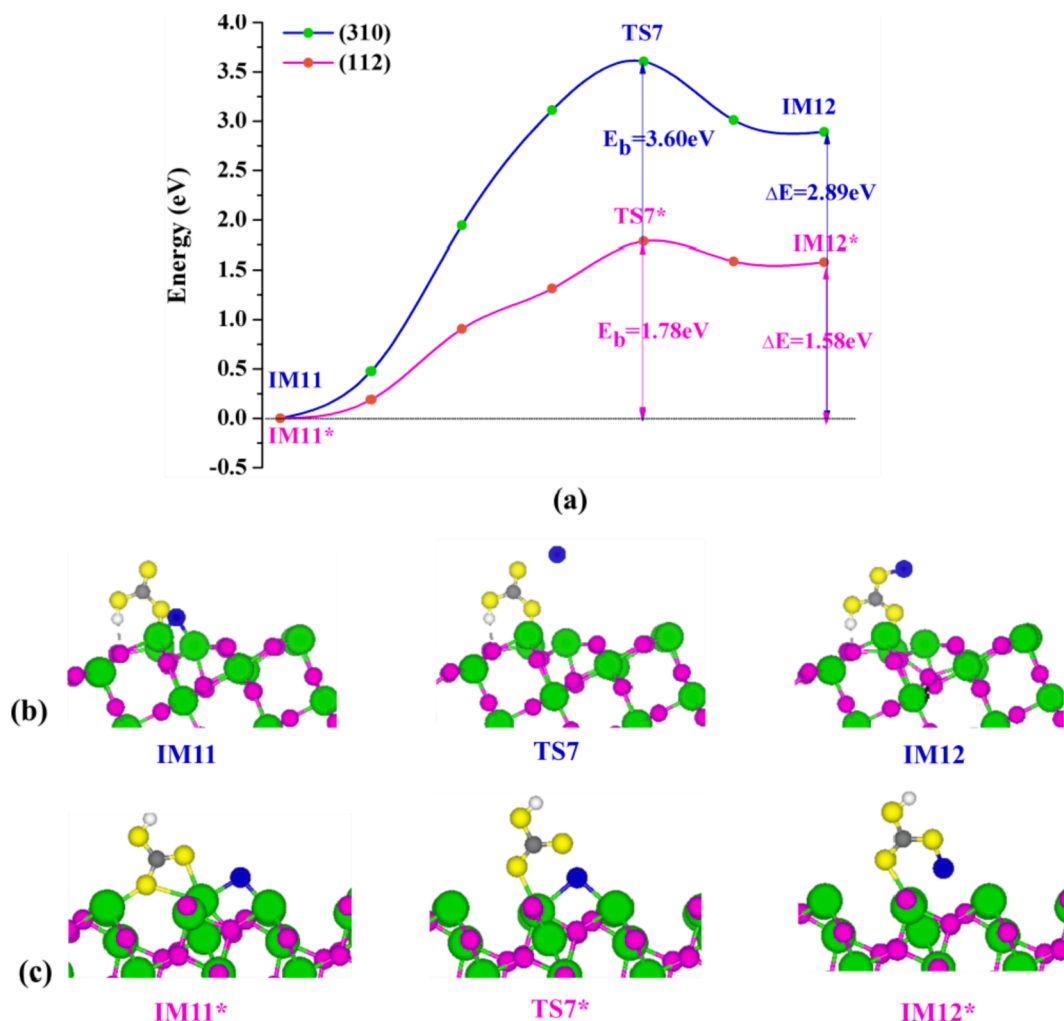


Fig. 6. (a) MEP plots for the pathway of $^*\text{HCO}_3 + ^*\text{O} \rightarrow ^*\text{HCO}_4$ on the (310) and (112) facets of SnO_2 . The side view of the intermediates and transition states along the paths on the (310) (b) and (112) (c) surfaces. The corresponding top views are shown in Figure S9. Sn and O are depicted as green and magenta spheres, respectively. The adsorbed C, O, and H atoms in HCO_3 group are grey, yellow and white respectively. The adsorbed O and H atoms in H_2O molecule are blue and white respectively.

calculated; the MEP plots and the involved intermediates and transition states are shown in Fig. 6. The energy barrier for the $^*\text{HCO}_3$ peroxidation is 1.78 and 3.60 eV on the (112) and (310) facets, respectively. The reaction is endothermic on both surfaces; the energies of the final states are 1.58 and 2.89 eV higher than those of the initial states on the (112) and (310) surfaces, respectively. This suggests, both thermodynamically and kinetically, that this reaction is not facile on these surfaces. Nevertheless, these calculation results are consistent with the experimental measurements. In the experimental tests, the measurable production of H_2O_2 only can be obtained at relatively high potentials (2.4–3.3 V vs RHE). [8,14,17] The standard potential at which HCO_3^- is oxidized to HCO_4^- is 1.80 V vs RHE. [43] This indicates that a high overpotential is needed for the peroxidation of HCO_3^- . In this work, the range of overpotentials to reach a current density of 5 mA/cm² is from 1.0 to 1.3 V for SnO_2 films tested in KHCO_3 with various concentrations (Fig. 5a). By comparison, our calculations show that the occurrence of this reaction is relatively easier on the (112) facet than that on the (310) facet, indicating that the (112) facet is kinetically favorable for $^*\text{HCO}_3$ peroxidation than the (310) facet. The adsorption energies of $^*\text{HCO}_3$ on the (112) and (310) planes are -1.96 and -3.04 eV, respectively. It is likely that the adsorption energy on the (310) facet is overly strong, which is not conducive to the peroxidation of $^*\text{HCO}_3$.

The hydrolyzation of the $^*\text{HCO}_4$ group on the (310) and (112) surfaces of SnO_2 are calculated as shown in Fig. 7. The reaction that

$^*\text{HCO}_4$ hydrolyzes to produce $^*\text{HCO}_3$ and $^*\text{H}_2\text{O}_2$ is assumed to be divided into two steps (Equations 13 and 14). First, $^*\text{HCO}_4$ and $^*\text{H}_2\text{O}$ interact to generate $^*\text{H}_2\text{CO}_4$. Second, $^*\text{H}_2\text{CO}_4$ and $^*\text{OH}$ combine to form $^*\text{HCO}_3$ and $^*\text{H}_2\text{O}_2$. As displayed in Fig. 7a, the interaction of $^*\text{HCO}_4$ and $^*\text{H}_2\text{O}$ to generate $^*\text{H}_2\text{CO}_4$ needs to overcome an energy barrier of 0.67 eV on the (112), while no energy barrier is needed on the (310) surface. The energy barrier of the second hydrolysis process on the (112) surface is 0.97 eV. Compared to the (112) surface, this process needs to conquer a high energy barrier of 2.73 eV on the (310) surface. Therefore, in terms of the energy barriers through the pathways that $^*\text{HCO}_3$ is oxidized and the subsequent hydrolysis process to generate $^*\text{H}_2\text{O}_2$, the (112) surface is kinetically more favorable than the (310) facet. The peroxidation of $^*\text{HCO}_3$ is the rate-determining step in the pathway of H_2O_2 formation in which $^*\text{HCO}_3$ participates. It is interesting and worth mentioning that $^*\text{H}_2\text{O}_2$ formed by the hydrolysis of $^*\text{HCO}_4$ can remain stable on the surface of SnO_2 . In experiment, the consumption of H_2O_2 on ZrO_2 was found to be considerably slower in the presence of HCO_3^- . [54] The mechanism for this phenomenon and the stabilizing effect of $^*\text{HCO}_3$ on $^*\text{H}_2\text{O}_2$ need to be further studied.

4. Conclusions

The H_2O_2 formation mechanisms on the (112) and (310) facets of SnO_2 via water oxidation reaction with and without the bicarbonate are

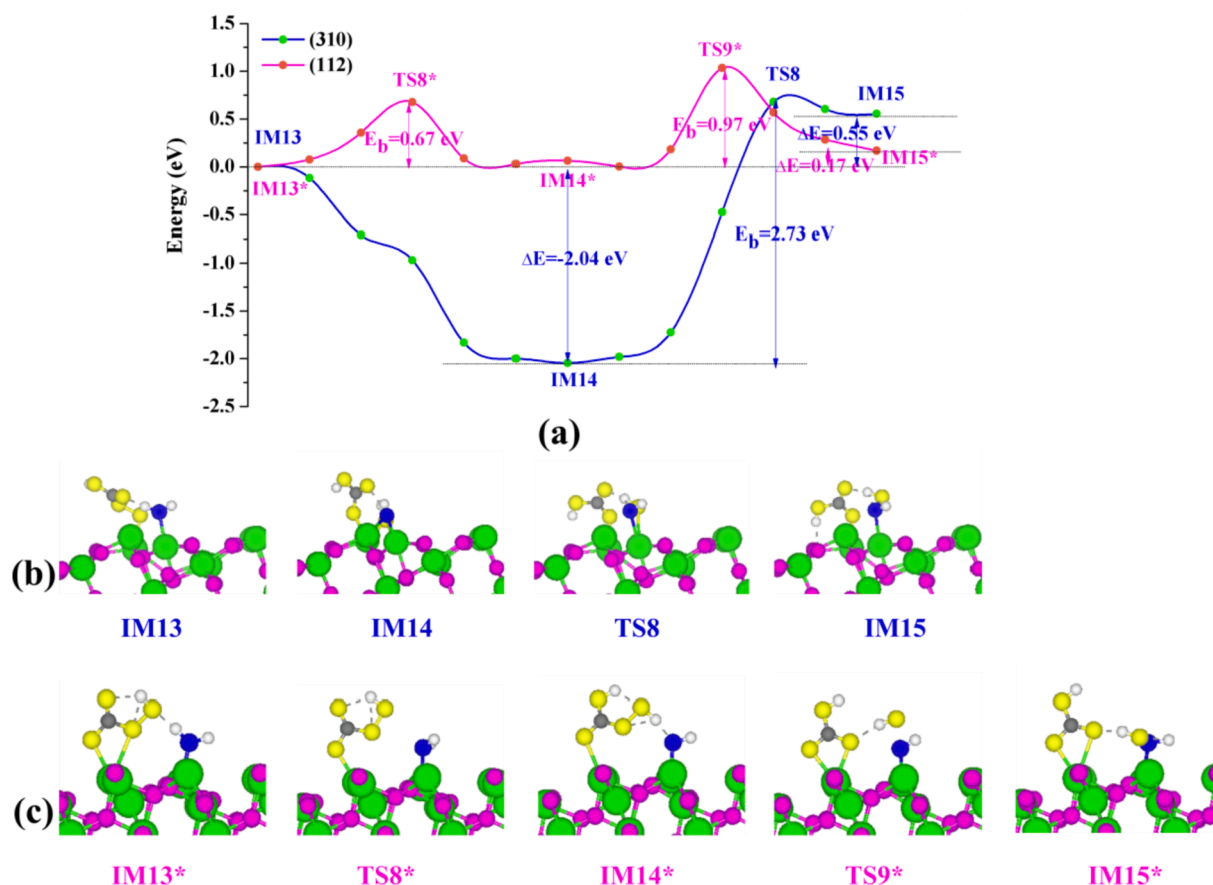


Fig. 7. (a) MEP plots for the pathway of ${}^*\text{HCO}_4 + {}^*\text{H}_2\text{O} \rightarrow {}^*\text{H}_2\text{CO}_4 + {}^*\text{OH} \rightarrow {}^*\text{HCO}_3 + {}^*\text{H}_2\text{O}_2$ on the (310) and (112) facets of SnO_2 . The side view of the intermediates and transition states along the paths on the (310) (b) and (112) surfaces (c). The corresponding top views are shown in Figure S10. Sn and O are depicted as green and magenta spheres, respectively. The adsorbed C, O, and H atoms in HCO_3 group are grey, yellow and white respectively. The adsorbed O and H atoms in H_2O molecule are blue and white respectively.

investigated using DFT calculations and electrochemical measurements. In the absence of HCO_3^- species, the H_2O_2 formation on SnO_2 through $2e^-$ WOR is difficult, that is, the O_2 evolution reaction via $4e^-$ WOR is predominant. The performance test of SnO_2 films confirms these calculations in that negligible H_2O_2 is generated in non-bicarbonate solutions after a period of chronoamperometry tests. In the presence of HCO_3^- species, the co-adsorption of HCO_3^- groups adjacent to the H_2O molecule could not significantly promote $2e^-$ WOR on the (112) and (310) surfaces. Considering that more H_2O_2 production is detected in KHCO_3 aqueous solution compared to those in non-bicarbonate electrolytes, it is reasonable that HCO_3^- directly participates in the generation process as a catalytic medium of H_2O_2 . The oxidation peaks in the LSV tested in KHCO_3 solutions indicate the formation of HCO_4^- during the electrochemical process. We therefore calculate the peroxidation of HCO_3^- species and the subsequent hydrolysis of HCO_4^- groups on the (112) and (310) surfaces of SnO_2 . While the energy barriers in these reaction pathways are relatively high, stable H_2O_2 is formed through these routes on both the (112) and (310) facets. The (112) surface of SnO_2 is more kinetically favorable for H_2O_2 generation compared to the (310) facet. Our work has deepened the understanding of the H_2O_2 formation mechanism in the presence of bicarbonate and provides insights into the design of catalysts for H_2O_2 generation that a suitable catalyst should have an appropriate adsorption for HCO_3^- and an effective catalytic ability for the peroxidation of HCO_3^- .

Author: Contributions

Wenlong Guo: Measurements, Characterization, DFT calculations, Writing.

Yinqiong Xie: Material synthesis.

Shi Tang: Material synthesis.

Bo Yu: Characterization.

Xin Lian: Measurements, DFT calculations, Writing.

Graeme Henkelman: DFT calculations.

Xi Liu: Measurements, DFT calculations, Writing.

We declare that we have no financial and personal relationships with other people or organizations that can inappropriately influence our work, there is no professional or other personal interest of any nature or kind in any product, service and/or company that could be construed as influencing the position presented in, or the review of, the manuscript entitled, " H_2O_2 Formation Mechanisms on the (112) and (310) Facets of SnO_2 via Water Oxidation Reaction with the Participation of Bicarbonate: DFT and Experimental Investigations".

Declaration of Competing Interest

The authors declare that they have no known competing financial interests or personal relationships that could have appeared to influence the work reported in this paper.

Acknowledgements

We gratefully acknowledge the Texas Advanced Computing Center and the Welch Foundation (F-1841) for computational resources, and funding from the National Natural Science Foundation of China (Grant No. 21903009 and 21908012) and the Natural Science Foundation of Chongqing (cstc2020jcyjmsxmX0735 and cstc2020jcyj-msxmX0875).

Appendix A. Supplementary data

Supplementary data to this article can be found online at <https://doi.org/10.1016/j.apsusc.2022.153634>.

References

- J. Tang, T. Zhao, D. Solanki, X. Miao, W. Zhou, S. Hu, Selective hydrogen peroxide conversion tailored by surface, interface, and device engineering, *Joule* 5 (6) (2021) 1432–1461.
- S. Mavrikis, S.C. Perry, P.K. Leung, L. Wang, C. Ponce de León, Recent Advances in Electrochemical Water Oxidation to Produce Hydrogen Peroxide: A Mechanistic Perspective, *ACS Sustainable Chemistry & Engineering* 9 (1) (2021) 76–91.
- J. Liu, Y. Zou, B. Jin, K. Zhang, J.H. Park, Hydrogen Peroxide Production from Solar Water Oxidation, *ACS Energy Letters* 4 (12) (2019) 3018–3027.
- S. Siahrostami, S.J. Villegas, A.H. Bagherzadeh Mostaghimi, S. Back, A.B. Farimani, H. Wang, K.A. Persson, J. Montoya, A Review on Challenges and Successes in Atomic-Scale Design of Catalysts for Electrochemical Synthesis of Hydrogen Peroxide, *ACS Catalysis* 10 (14) (2020) 7495–7511.
- Y. Xue, Y. Wang, Z. Pan, K. Sayama, Electrochemical and Photoelectrochemical Water Oxidation for Hydrogen Peroxide Production, *Angew. Chem. Int. Ed. Engl.* 60 (19) (2021) 10469–10480.
- C. Xia, Y. Xia, P. Zhu, L. Fan, H. Wang, Direct Electrosynthesis of Pure Aqueous H₂O₂ Solutions up to 20% by Weight Using a Solid Electrolyte, *Science* 366 (6462) (2019) 226–231.
- S.C. Perry, D. Pangotra, L. Vieira, L.I. Csepei, V. Sieber, L. Wang, C. Ponce de León, F.C. Walsh, Electrochemical Synthesis of Hydrogen Peroxide from Water and Oxygen, *Nature Reviews, Chemistry* 3 (2019) 442–458.
- Y. Wang, X. Lian, Y. Zhou, W.L. Guo, H.C. He, Synthesis and Characterization of Sb₂O₃: A Stable Electrocatalyst for Efficient H₂O₂ Production and Accumulation and Effective Degradation of Dyes, *New Journal of Chemistry* 45 (2021) 8958–8964.
- C. Xia, S. Back, S. Ringe, K. Jiang, F.H. Chen, X.M. Sun, S. Siahrostami, K. Chan, H. T. Wang, Confined Local Oxygen Gas Promotes Electrochemical Water Oxidation to Hydrogen Peroxide, *Nature Catalysis* 3 (2020) 125–134.
- S. Mavrikis, M. Göltz, S.C. Perry, F. Bogdan, P.K. Leung, S. Rosiwal, L. Wang, C. Ponce de León, Effective Hydrogen Peroxide Production from Electrochemical Water Oxidation, *ACS Energy Lett.* 6 (2021) 2369–2377.
- X.J. Shi, S. Back, T.M. Gill, S. Siahrostami, X.L. Zheng, Electrochemical Synthesis of H₂O₂ by Two-Electron Water Oxidation Reaction, *Chem* 7 (2021) 38–63.
- Y.Y. Sun, L. Han, P. Strasser, A Comparative Perspective of Electrochemical and Photochemical Approaches for Catalytic H₂O₂ Production, *Chem. Soc. Rev.* 49 (2020) 6605.
- A. Izgorodin, E. Izgorodina, D.R. MacFarlane, Low overpotential water oxidation to hydrogen peroxide on a MnO_x catalyst, *Energy & Environmental Science* 5 (11) (2012) 9496, <https://doi.org/10.1039/c2ee21832a>.
- X. Shi, S. Siahrostami, G.L. Li, Y. Zhang, P. Chakthranont, F. Studt, T.F. Jaramillo, X. Zheng, J.K. Nørskov, Understanding activity trends in electrochemical water oxidation to form hydrogen peroxide, *Nat Commun.* 8 (1) (2017) 701.
- K. Fuku, Y. Miyase, Y. Miseki, T. Gunji, K. Sayama, Enhanced Oxidative Hydrogen Peroxide Production on Conducting Glass Anodes Modified with Metal Oxides, *Chemistry Select* 1 (18) (2016) 5721–5726.
- S.-G. Xue, L.u. Tang, Y.-K. Tang, C.-X. Li, M.-I. Li, J.-j. Zhou, W. Chen, F. Zhu, J. Jiang, Selective Electrocatalytic Water Oxidation to Produce H₂O₂ Using a C, N Codoped TiO₂ Electrode in an Acidic Electrolyte, *ACS Appl Mater Interfaces* 12 (4) (2020) 4423–4431.
- S.R. Kelly, X. Shi, S. Back, L. Vallez, S.Y. Park, S. Siahrostami, X. Zheng, J. K. Nørskov, ZnO As an Active and Selective Catalyst for Electrochemical Water Oxidation to Hydrogen Peroxide, *ACS Catalysis* 9 (5) (2019) 4593–4599.
- C. Zhang, J. Lu, C. Liu, Y. Zou, L. Yuan, J. Wang, C. Yu, ZnO nanoparticles embedded in hollow carbon fiber membrane for electrochemical H₂O₂ production by two-electron water oxidation reaction, *Environmental Research* 206 (2022) 112290, <https://doi.org/10.1016/j.envres.2021.112290>.
- A. Nadar, S.S. Gupta, Y. Kar, S. Shetty, A.P. van Bavel, D. Khushalani, Evaluating the Reactivity of BiVO₄ Surfaces for Efficient Electrocatalytic H₂O₂ Production: A Combined Experimental and Computational Study, *The Journal of Physical Chemistry C* 124 (7) (2020) 4152–4161.
- J.H. Baek, T.M. Gill, H. Abroshan, S. Park, X. Shi, J. Nørskov, H.S. Jung, S. Siahrostami, X. Zheng, Selective and Efficient Gd-Doped BiVO₄ Photoanode for Two-Electron Water Oxidation to H₂O₂, *ACS Energy Letters* 4 (3) (2019) 720–728.
- X. Shi, Y. Zhang, S. Siahrostami, X. Zheng, Light-Driven BiVO₄-C Fuel Cell with Simultaneous Production of H₂O₂, *Advanced Energy Materials* 8 (23) (2018) 1801158, <https://doi.org/10.1002/aenm.v8.2310.1002/aenm.201801158>.
- K. Fuku, Y. Miyase, Y. Miseki, T. Gunji, K. Sayama, WO₃/BiVO₄ photoanode coated with mesoporous Al₂O₃ layer for oxidative production of hydrogen peroxide from water with high selectivity, *RSC Adv.* 7 (75) (2017) 47619–47623.
- Y. Miyase, S. Iguchi, Y. Miseki, T. Gunji, K. Sayama, Electrochemical H₂O₂ Production and Accumulation from H₂O by Composite Effect of Al₂O₃ and BiVO₄, *The Electrochemical Society* 166 (13) (2019) H644–H649.
- K. Zhang, J. Liu, L. Wang, B. Jin, X. Yang, S. Zhang, J.H. Park, Near-Complete Suppression of Oxygen Evolution for Photoelectrochemical H₂O Oxidative H₂O₂ Synthesis, *J. Am. Chem. Soc.* 142 (19) (2020) 8641–8648.
- S.Y. Park, H. Abroshan, X. Shi, H.S. Jung, S. Siahrostami, X. Zheng, CaSnO₃: An Electrocatalyst for Two-Electron Water Oxidation Reaction to Form H₂O₂, *ACS Energy Letters* 4 (1) (2019) 352–357.
- T. Kang, B. Li, Q. Hao, W. Gao, F. Bin, K.N. Hui, D. Fu, B. Dou, Efficient Hydrogen Peroxide (H₂O₂) Synthesis by CaSnO₃ via Two-Electron Water Oxidation Reaction, *ACS Sustainable Chemistry & Engineering* 8 (39) (2020) 15005–15012.
- L. Li, Z. Hu, J.C. Yu, On-Demand Synthesis of H₂O₂ by Water Oxidation for Sustainable Resource Production and Organic Pollutant Degradation, *Angew. Chem. Int. Ed. Engl.* 59 (46) (2020) 20538–20544.
- K. Fuku, K. Sayama, Efficient oxidative hydrogen peroxide production and accumulation in photoelectrochemical water splitting using a tungsten trioxide/bismuth vanadate photoanode, *Chem. Commun.* 52 (31) (2016) 5406–5409.
- Y. Lai, X. Liu, H. Ye, G. Ke, B. Lui, F. Dong, H. He, Objective Observations of the Electrochemical Production of H₂O₂ in KHCO₃ Aqueous Electrolyte and Related Application Inspirations, *The Journal of Physical Chemistry C* 125 (36) (2021) 19831–19838.
- T.M. Gill, L. Vallez, X. Zheng, The Role of Bicarbonate-Based Electrolytes in H₂O₂ Production through Two-Electron Water Oxidation, *ACS Energy Letters* 6 (8) (2021) 2854–2862.
- V. Viswanathan, H.A. Hansen, J.K. Nørskov, Selective Electrochemical Generation of Hydrogen Peroxide from Water Oxidation, *J. Phys. Chem. Lett.* 6 (21) (2015) 4224–4228.
- G. Kresse, J. Hafner, Ab Initio Molecular Dynamics for Liquid Metals, *Phys. Rev. B: Condens. Matter Mater. Phys.* 47 (1993) 558–561.
- G. Kresse, J. Hafner, Ab Initio Molecular-Dynamics Simulation of The Liquid-Metal–Amorphous-Semiconductor Transition in Germanium, *Phys. Rev. B: Condens. Matter Mater. Phys.* 49 (1994) 14251–14269.
- G. Kresse, J. Furthmüller, Efficiency of Ab-Initio Total Energy Calculations for Metals and Semiconductors Using a Plane-Wave Basis Set, *Comput. Mater. Sci.* 6 (1) (1996) 15–50.
- P.E. Blöchl, Projector Augmented-Wave Method, *Phys. Rev. B: Condens. Matter Mater. Phys.* 50 (1994) 17953–17979.
- G. Kresse, D. Joubert, From Ultrasoft Pseudopotentials to The Projector Augmented-Wave Method, *Phys. Rev. B: Condens. Matter Mater. Phys.* 59 (3) (1999) 1758–1775.
- G. Kresse, J. Furthmüller, Efficient Iterative Schemes for ab initio Total-Energy Calculations Using a Plane-Wave Basis Set, *Phys. Rev. B: Condens. Matter Mater. Phys.* 54 (16) (1996) 11169–11186.
- J.P. Perdew, K. Burke, M. Ernzerhof, Generalized Gradient Approximation Made Simple, *Phys. Rev. Lett.* 77 (1996) 3865–3868.
- H.J. Monkhorst, J.D. Pack, Special Points for Brillouin-Zone Integrations, *Phys. Rev. B* 13 (1976) 5188–5192.
- G. Henkelman, B.P. Uberuaga, H. Jonsson, A Climbing Image Nudged Elastic Band Method for Finding Saddle Points and Minimum Energy Paths, *J. Chem. Phys.* 113 (2000) 9901–9904.
- M.-T. Nguyen, N. Seriani, S. Piccinin, R. Gebauer, Photo-Driven Oxidation of Water on α -Fe₂O₃ Surfaces: an ab initio Study, *J. Chem. Phys.* 140 (6) (2014) 064703, <https://doi.org/10.1063/1.4865103>.
- W.L. Guo, X. Lian, Kinetics mechanism insights into the oxygen evolution reaction on the (110) and (022) crystal facets of β -Cu₂V₂O₇, *Catal. Sci. Technol.* 10 (2020) 5129–5135.
- D.E. Richardson, H. Yao, K.M. Frank, D.A. Bennett, Equilibria, kinetics, and mechanism in the bicarbonate activation of hydrogen peroxide: oxidation of sulfides by peroxymonocarbonate, *J. Am. Chem. Soc.* 122 (2000) 1729–1739.
- H.B. Wu, J.S. Chen, X.W. Lou, H.H. Hng, Synthesis of SnO₂ Hierarchical Structures Assembled from Nanosheets and Their Lithium Storage Properties, *The Journal of Physical Chemistry C* 115 (50) (2011) 24605–24610.
- S.Y. Zhao, C.X. Li, J. Liu, N.Y. Liu, S. Qiao, Y.Z. Han, H. Huang, Y. Liu, Z.H. Kang, Carbon quantum dots/SnO₂-Co₃O₄ composite for highly efficient electrochemical water oxidation, *Carbon* 92 (2015) 64–73.
- J. Szubera, G. Czempika, R. Larcipreteb, D. Kozieja, B. Adamowicz, XPS study of the L-CVD deposited SnO₂ thin films exposed to oxygen and hydrogen, *Thin Solid Films* 391 (2001) 198–203.
- H. Ye, L. Yang, X. Nie, K. Liu, S. Yang, Y. Zhou, F. Dong, H. He, H. Yang, Dual-functional water splitting: Electro-fenton-like pollutants degradation from anode reaction and hydrogen fuel production from cathode reaction, *Electrochimica Acta* 394 (2021) 139122, <https://doi.org/10.1016/j.electacta.2021.139122>.
- K. Dong, J. Liang, Y.Y. Wang, Y.C. Ren, Z.Q. Xu, H.P. Zhou, L. Li, Q. Liu, Y.L. Luo, T.S. Li, A.M. Asiri, Q. Li, D.W. Ma, X.P. Sun, Plasma-induced defective TiO_{2-x} with oxygen vacancies: A high-active and robust bifunctional catalyst toward H₂O₂ electrosynthesis, *Chem Catalysis* 1 (2021) 1437–1448.
- X. Huang, M. Song, J. Zhang, J. Zhang, W. Liu, C. Zhang, W. Zhang, D. Wang, Investigation of MXenes as oxygen reduction electrocatalyst for selective H₂O₂ generation, *Nano Res.* 15 (5) (2022) 3927–3932, <https://doi.org/10.1007/s12274-021-4057-9>.
- Q. Chen, C. Ma, S. Yan, J. Liang, K. Dong, Y. Luo, Q. Liu, T. Li, Y. Wang, L. Yue, B. Zheng, Y. Liu, S. Gao, Z. Jiang, W. Li, X. Sun, Greatly Facilitated Two-Electron Electroreduction of Oxygen into Hydrogen Peroxide over TiO₂ by Mn Doping, *ACS Appl. Mater. Interfaces* 13 (39) (2021) 46659–46664.
- Z.Q. Deng, C.Q. Ma, et al., One-dimensional conductive metal–organic framework nanorods: a highly selective electrocatalyst for the oxygen reduction to hydrogen peroxide, *J. Mater. Chem. A* 9 (2021) 20345–20349.

- [52] Z.Q. Xu, J. Liang, et al., Enhanced Electrochemical H₂O₂ Production via Two-Electron Oxygen Reduction Enabled by Surface-Derived Amorphous Oxygen-Deficient TiO_{2-x}, *ACS Appl. Mater. Interfaces* 13 (2021) 33182–33187.
- [53] K. Dong, J. Liang, Y. Ren, Y. Wang, Z. Xu, L. Yue, T. Li, Q. Liu, Y. Luo, Y. Liu, S. Gao, M.S. Hamdy, Q. Li, D. Ma, X. Sun, Electrochemical two-electron O₂ reduction reaction toward H₂O₂ production: using cobalt porphyrin decorated carbon nanotubes as a nanohybrid catalyst, *J. Mater. Chem. A* 9 (46) (2021) 26019–26027.
- [54] E. Toijer, M. Jonsson, Anion effects on the catalytic decomposition of H₂O₂ on ZrO₂(s) in aqueous systems, *ChemistrySelect* 5 (43) (2020) 13754–13760.